

Article

Polydopamine-Modified Carboxymethyl Cellulose as Advanced Polysulfide Trapping Binder

Daniel A. Gribble * and Vilas G. Pol *

Davidson School of Chemical Engineering, Purdue University, West Lafayette, IN 47907, USA

* Correspondence: dgribbl@purdue.edu (D.A.G.); vpol@purdue.edu (V.G.P.)

Abstract: The search for a high-energy-density alternative to lithium-ion batteries has led to great interest in the lithium sulfur battery (LSB). However, poor cycle lifetimes and coulombic efficiencies (CEs) due to detrimental lithium polysulfide (LiPS) shuttling has hindered its widespread adoption. To address this challenge, a modified sodium carboxymethyl cellulose (CMC) polymer with integrated dopamine moieties and polydopamine nanoparticles was created through a facile one-pot dopamine (DOP) amidation reaction to strengthen noncovalent interactions with LiPSs and mitigate the shuttling effect. The resulting CMC-DOP binder improved electrode wettability, adhesion, and electrochemical performance. Compared to LSBs with a standard CMC binder, CMC-DOP 5:1 (with a 5:1 weight ratio of CMC to dopamine precursor) improves the specific capacity at cycle 100 by 38% to 552 mAh g⁻¹ and CE from 96.8 to 98.9%. LSBs show good stability, even after 500 cycles. Post-mortem electrochemical impedance spectroscopy (EIS) and energy-dispersive spectroscopy (EDS) studies confirmed the effectiveness of the CMC-DOP in confining LiPS in the cathode. This simple but effective nature-inspired strategy promises to enhance the viability of LSBs without using harmful chemicals or adding excess bulk.

Keywords: functional binder; carboxymethyl cellulose; polydopamine; one-pot synthesis; lithium sulfur battery; shuttle effect; aqueous binder



Citation: Gribble, D.A.; Pol, V.G. Polydopamine-Modified Carboxymethyl Cellulose as Advanced Polysulfide Trapping Binder. *Batteries* **2023**, *9*, 525. <https://doi.org/10.3390/batteries9110525>

Academic Editor: Yushi He

Received: 17 September 2023

Revised: 19 October 2023

Accepted: 20 October 2023

Published: 24 October 2023



Copyright: © 2023 by the authors. Licensee MDPI, Basel, Switzerland. This article is an open access article distributed under the terms and conditions of the Creative Commons Attribution (CC BY) license (<https://creativecommons.org/licenses/by/4.0/>).

1. Introduction

Stagnating innovation in lithium-ion batteries (LIBs) and movement towards electrification has sparked a search for new electrode materials [1,2]. Further improvement in the energy density of state-of-the-art LIBs is limited by the theoretical capacity of the graphite anode and metal oxide cathode [3]. The transformative effect higher energy density batteries could have therefore led to extensive research on alternative materials for rechargeable batteries [4,5]. Lithium sulfur batteries (LSBs) have emerged as a leading area of investigation since sulfur cathodes offer a theoretical capacity of 1675 mAh g⁻¹, whereas lithium cobalt oxide cathodes offer a maximum of 274 mAh g⁻¹ [6]. LSBs are often additionally paired with a lithium metal anode, which is unmatched in terms of its energy density [7]. Sulfur is also more abundant and economical than cobalt [1,8]. Despite these advantages, there are still fundamental challenges to be addressed before LSBs are marketable.

The two main challenges with LSBs are low electronic conductivity of elemental sulfur and the shuttling of lithium polysulfides (LiPS). Poor electron transfer through sulfur limits the practical capacity of the cathode, resulting in high overpotentials and low active material utilization. The migration of soluble LiPS intermediaries to the lithium anode also causes the formation of unfavorable solid-electrolyte interphases (SEI), high impedances, active material loss, and poor cycle lifetimes [1,9,10]. To address these issues, researchers have composited sulfur with carbon to provide a high surface area and electrical conductivity for increased sulfur utilization. Carbon also shows a moderate affinity for LiPS species, thereby improving both the capacity and capacity retention [9–12]. Further advances are needed, however, to meet the energy densities and cycle lifetimes required

for practical applications. Synergistic strategies such as active material coatings [13,14] and modified separators [15–17] have demonstrated efficacy, but come with the drawback of lower volumetric and gravimetric energy densities due to the inclusion of electrochemically inactive species.

An alternative solution is to use a multifunctional polymer binder, which offers the advantage of not adding unnecessary weight or bulk [18,19]. These polymers can be grafted with various nucleophilic functional groups such as carboxylates, alcohols, or amines which strongly interact with LiPS and hinder their diffusion and migration out of the porous cathode [20]. Some of the polymers studied for this purpose include polyvinyl alcohol, polyvinyl pyrrolidone, polyacrylic acid, and sodium carboxymethyl cellulose (CMC) [20–24]. As a water soluble polymer, CMC has seen much interest in battery research for its low environmental impact and sustainability. Its versatile functional groups and tunable structure has led to applications as a platform for multifunctional binders and ion conducting membranes [25–27].

Bio-inspired polydopamine (PD) is also known for its strong non-covalent interactions and metal chelating capabilities [28,29]. PD has proven to be effective as an LSB active material coating [30], as well as a separator coating to confine LiPS in the cathode and improve surface properties [15]. The oxidative self-polymerization of dopamine into PD is facilitated by a weakly alkaline buffer solution [31]. However, preparing PD requires several steps including addition, separation, and purification.

This study improves the polysulfide trapping abilities and physical properties of CMC-based binder by modifying it with dopamine. The composite binder is synthesized through a simple one-pot aqueous reaction, enhancing its LiPS affinity. The thermal amidation and substitution reaction produces CMC modified with dopamine moieties and PD nanoparticles without the need for purification. The resulting CMC-DOP composite binder demonstrates improved adhesion, wettability, and LiPS retention compared to standard CMC. Optimal electrochemical performance is observed with a 5:1 weight ratio of CMC to dopamine precursor in LSB full cells. Galvanostatic cycling of LSBs with CMC-DOP 5:1 binder at cycle 100 shows 38% improvement in specific capacity over CMC from 399 to 552 mAh g^{-1} , enhanced average coulombic efficiency (CE) from 96.9 to 98.7%, and lower SEI resistance in electrochemical impedance spectroscopy (EIS) investigations. Post-mortem energy dispersive spectroscopy (EDS) analyses mechanistically support sulfur confinement at the cathode. This strategy provides a simple and effective way to enhance the viability of LSBs without using harmful chemicals or adding bulk. Further improvements can be made by combining the binder system with corrosion-inhibiting current collectors.

2. Results and Discussion

2.1. Synthesis

Dopamine-modified carboxymethyl cellulose binder (CMC-DOP) was synthesized in a simple one-pot thermal amidation reaction. In a slurry cup, CMC and dopamine HCl precursor are dissolved in water. The clear aqueous solution is then transferred to a sealed Teflon autoclave reactor and heated to 100°C for 24 h. FTIR spectra of precursors and binder solutions before and after the reaction are shown in Figure 1a. Successful acidification of Na carboxylate on CMC and CMC/DOP 2:1 into carboxylic acid in CMC-DOP 2:1 is evidenced by a new peak at 1725 cm^{-1} , which corresponds to the C=O stretching of the newly formed COOH group, as well as the diminished asymmetric and symmetric COO^- stretching band at 1585 and 1410 cm^{-1} , respectively [32,33]. Thermal amidation of the carboxyl groups occurs via self-oxidation of dopamine under acidic conditions, creating dopamine moieties grafted to the CMC backbone (Figure S1) [32,34]. Evidence of successful amidation is evidenced by a color change of CMC/DOP solutions from clear to dark brown (Figure 1b) [35,36]. FTIR results herein are consistent with previously reported dopamine-functionalized CMC [34].

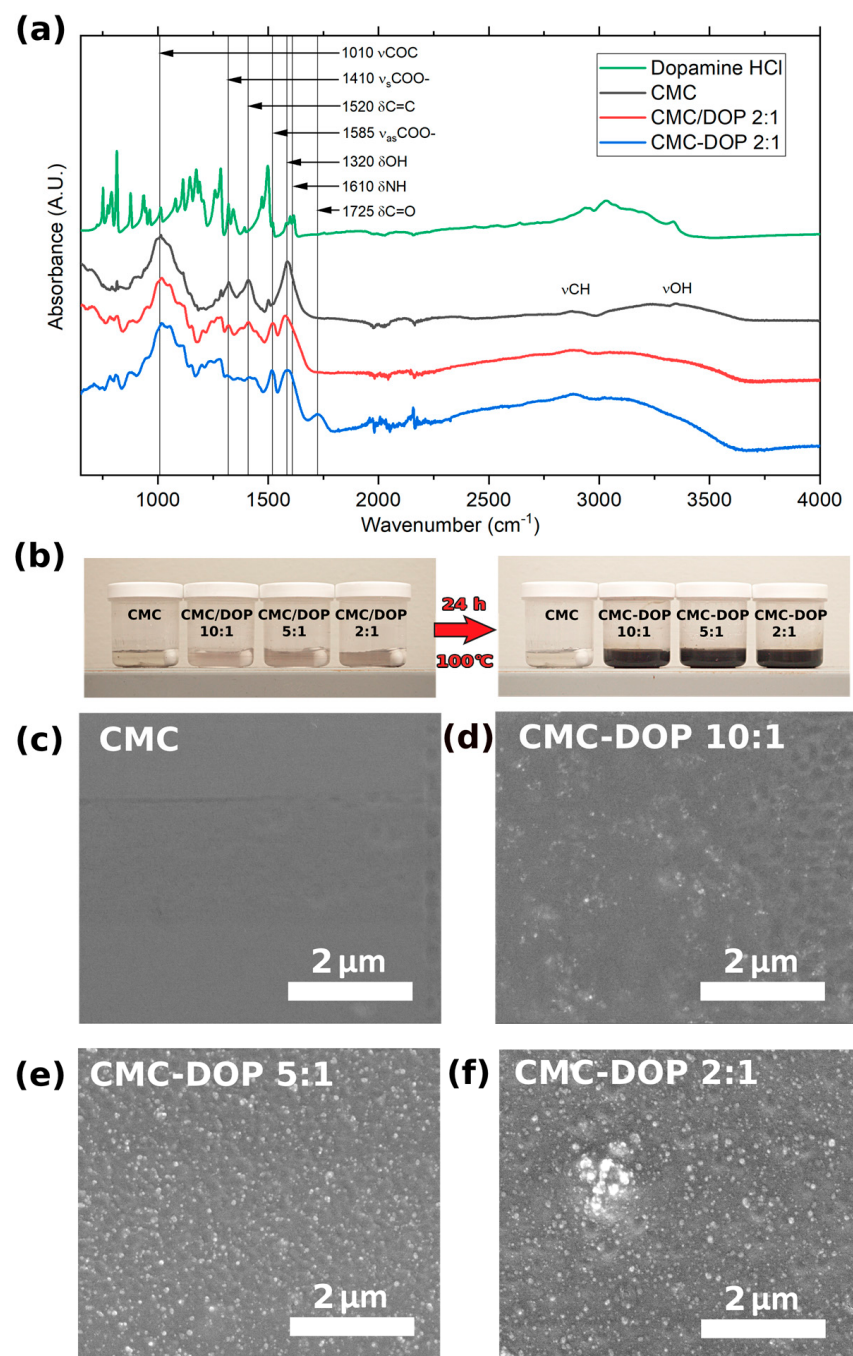


Figure 1. (a) FTIR spectra of precursors and binders. (b) Photos showing the change in color of binder solutions before and after amidation reaction. (c–f) SEM images of prepared binders cast on foil.

Despite the clear visual transformation, NH bending at 1610 cm^{-1} evident in dopamine HCl precursor cannot be resolved due to overlap with the strong and wide COO^- peak at 1585 cm^{-1} [32,34]. Visible in all FTIR spectra except CMC, however, are peaks at 1520 cm^{-1} which correspond to C=C stretching in the aromatic ring of dopamine [37]. Despite the high ratio of dopamine precursor in CMC/DOP 2:1 mixture as well as reacted CMC-DOP 2:1, strong C signals still mask the amine and amide groups. The integrity of the polymer backbone is verified by heating a CMC solution at 100°C for 72 h (Figure S2). After this time elapsed, there are no significant changes which would indicate degradation, such as the thermal breakdown into formate. This is supported by negligible changes in the peak at 1010 cm^{-1} corresponding to the COC bonds in the CMC backbone after heating (Figure 1a) [34]. These findings are consistent with the literature expectations [38].

Typically, oxidative polymerization of dopamine requires an alkaline environment [31]. To protect the precursor from unwanted reactions, it is stabilized as dopamine HCl salt by the manufacturer. However, heat-activated polymerization of dopamine into PD in acidic solutions has been previously reported [39]. This is likely aided by the carboxyl substitution as well. It is evident that excess dopamine precursor leads to the formation of PD in addition to grafted dopamine moieties. HR-SEM images of CMC, CMC-DOP 10:1, CMC-DOP 5:1, and CMC-DOP 2:1 films are shown in Figure 1c–f. In contrast to the heterogeneous CMC film, the CMC-DOP films show the presence of small, well-dispersed nanoparticles. The size and morphology of the particles are consistent with previous studies on solution synthesis of PD nanoparticles, providing strong evidence of concurrent PD formation [31,39]. Further, the quantity of the particles increases with the increasing amount of dopamine precursor. A detailed analysis of the images (Figures S3 and S4) reveals that all the prepared binders have PD particles of roughly the same size, at 49.5 ± 21.9 , 52.1 ± 17.1 , and 53.5 ± 23.6 nm for CMC-DOP 10:1, 5:1, and 2:1, respectively (Table S1). This also reveals that 5:1 has the most regular morphology and narrowest standard deviation of particle size. Despite an approximately two-fold increase in the amount of precursor in CMC-DOP 10:1 to 5:1, we observe an approximately four-fold increase in the number of particles, showcasing the effect of adding excess precursor (Table S1). We can also observe additional irregularities for CMC-DOP 2:1, which has started to aggregate PD into larger micron-scale secondary particles (Figure 1f). Larger particles and aggregates would decrease the effective surface area per mass of the PD, hindering its ability to interact with the LiPS. Due to the ratio of the components, the relatively strong carbon signal of CMC, and peak overlap, we are still unable to identify the PD in the FTIR spectrum, however, despite clear evidence of its presence in the HR-SEM images.

2.2. Electrode Characterizations

S cathodes are prepared by combining the aqueous binder dispersion with S/C composite and blade-coating. The resulting electrodes have an active loading of approximately 1 mg cm^{-2} and binder ratio of 15 wt.%. SEM images with overlayed EDS mapping of the electrodes are shown in Figure 2, where S, Na, and Cl are represented by the colors yellow, red, and blue, respectively. Immediately noticeable is the low S intensity for CMC-DOP 2:1 (Figure 2d). Enhanced surfactance of the electrode composite enabled by the CMC-DOP may more thoroughly coat the S and larger graphene composite particles. This is supported by a trend of decreasing apparent S wt.% as measured with the EDS quantitative analysis with the increasing PD ratio. Results show 13.7, 12.7, 12.6, and 8.3 wt.% S for CMC and CMC-DOP 10:1, 5:1, and 2:1 electrodes, respectively (Table S2). It is also likely that a thin NaCl coating over the electrode lowers the apparent S intensity. Also noticeable in the mapping for CMC-DOP 2:1 electrode are purple particles 5–10 μm in size corresponding to NaCl that has precipitated upon drying as a byproduct of the acidification of the Na carboxylate functional group. Compared to the standard CMC electrode, the CMC-DOP electrodes show micron-sized holes distributed throughout. This is likely an effect of residual HCl corroding the Al foil and evolving H_2 gas. Assuming equimolar quantities of dopamine and HCl as well as the complete dissociation of HCl, this would form acidic solutions with pHs of 2.01, 1.75, and 1.41 for CMC-DOP 10:1, 5:1, and 2:1, respectively, in the binder solution. SEM/EDS of the reverse side of the electrode foil shows signs of corrosion with corresponding intensities from Cl and O for the CMC-DOP electrodes (Figures S5–S8). The comparatively high intensity of O suggests that hygroscopic AlCl_3 has formed hexahydrate $[\text{Al}(\text{H}_2\text{O})_6]\text{Cl}_3$. This can potentially add weight to the current collector and result in the underestimation of the specific capacity in later cycling studies. It is worth noting in passing that CMC can mitigate the corrosive effect of HCl on the Al foil [40].

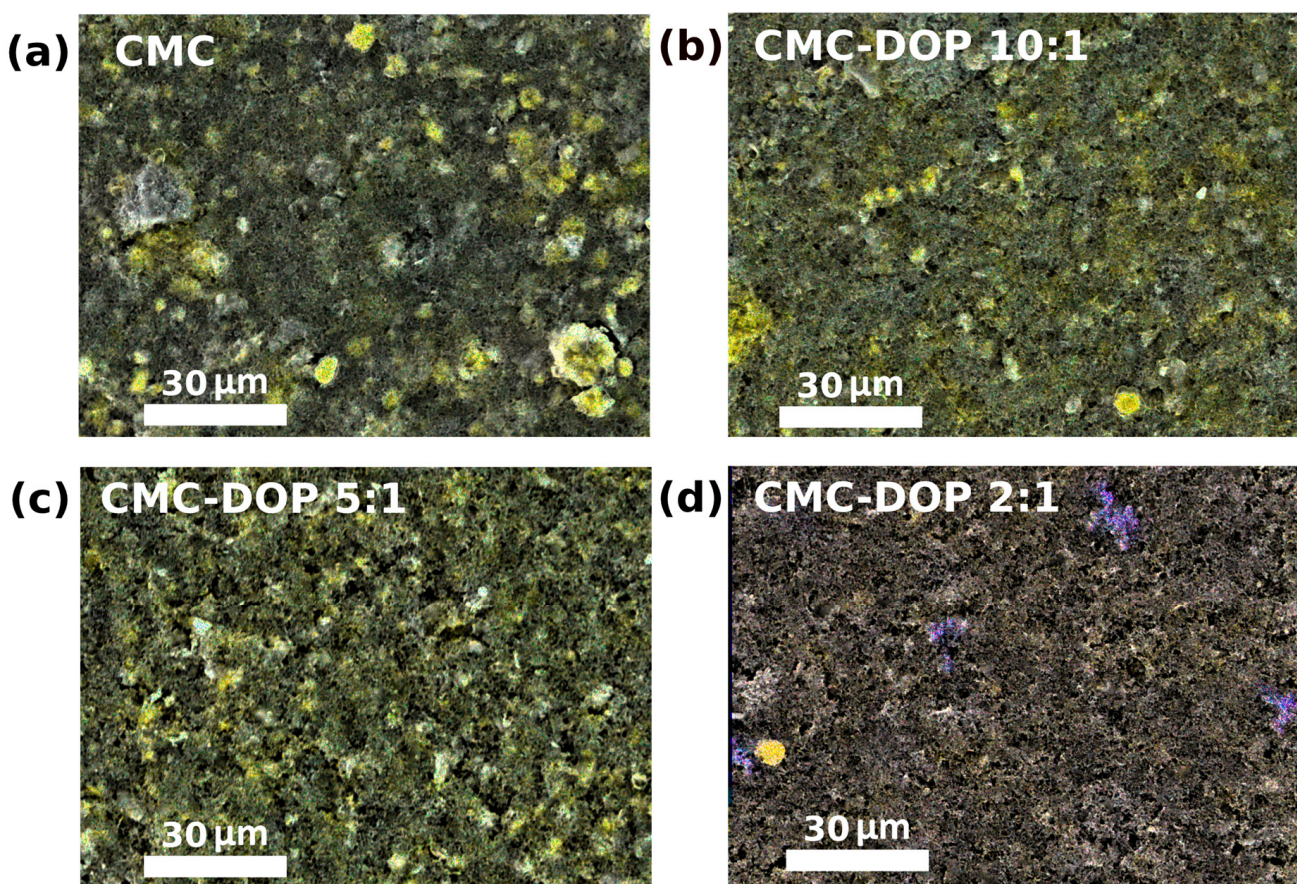


Figure 2. SEM images prepared composite cathodes with overlayed EDS mapping of S (Yellow), Na (Red), and Cl (Blue) for (a) CMC, (b) CMC-DOP 10:1, (c) CMC-DOP 5:1, and (d) CMC-DOP 2:1.

Dopamine integrated into the electrode is demonstrated to enhance its physical properties [34]. Poor electrode wettability can hinder the electrolyte permeation, resulting in high impedances and poor electrochemical performance. It may also complicate the manufacturing process by requiring longer times for electrolyte filling [41]. Strongly polar catechol groups can interact with polar electrolyte solvents and improve wettability. This is demonstrated in Figure 3a–d, which shows contact-angle measurements for a liquid droplet on the prepared S/C composite electrodes. Water was used in place of the DOL:DME solvent since low viscosity of the ethers resulted in rapid adsorption of the droplet, which complicated quantitative measurements. A smaller contact-angle indicates good wettability and high compatibility of the electrode and electrolyte [18]. For S/C electrodes with CMC and CMC-DOP 10:1, 5:1, and 2:1 binders, we observe contact-angles of 43°, 35°, 29°, and 23°, respectively. Results are consistent with findings from similar investigations [34]. In electrochemical tests, good electrolyte contact may facilitate good ion conduction, low impedances, and high active material utilization [41].

PD is a bio-inspired polymer adhesive adapted from the glue mussels used to adhere to rocks [28,29]. Its application in electrodes may similarly provide advantages in mechanical properties. Figure 3e shows results of a tape-peel test. Cellulose tape was placed on top of the S/C composite electrode and adhered by rolling a 1 kg cylindrical weight over the surface. The tape was then peeled off, removing some of the composite electrode in the process. It is visually evident that PD is effective in enhancing adhesion of the S/C composite to the current collector, with the effect increasing with dopamine ratio. Enhanced adhesion can facilitate higher capacity retention by mitigating the delamination of active materials from the current collector and the formation of electronically isolated dead material [42,43].

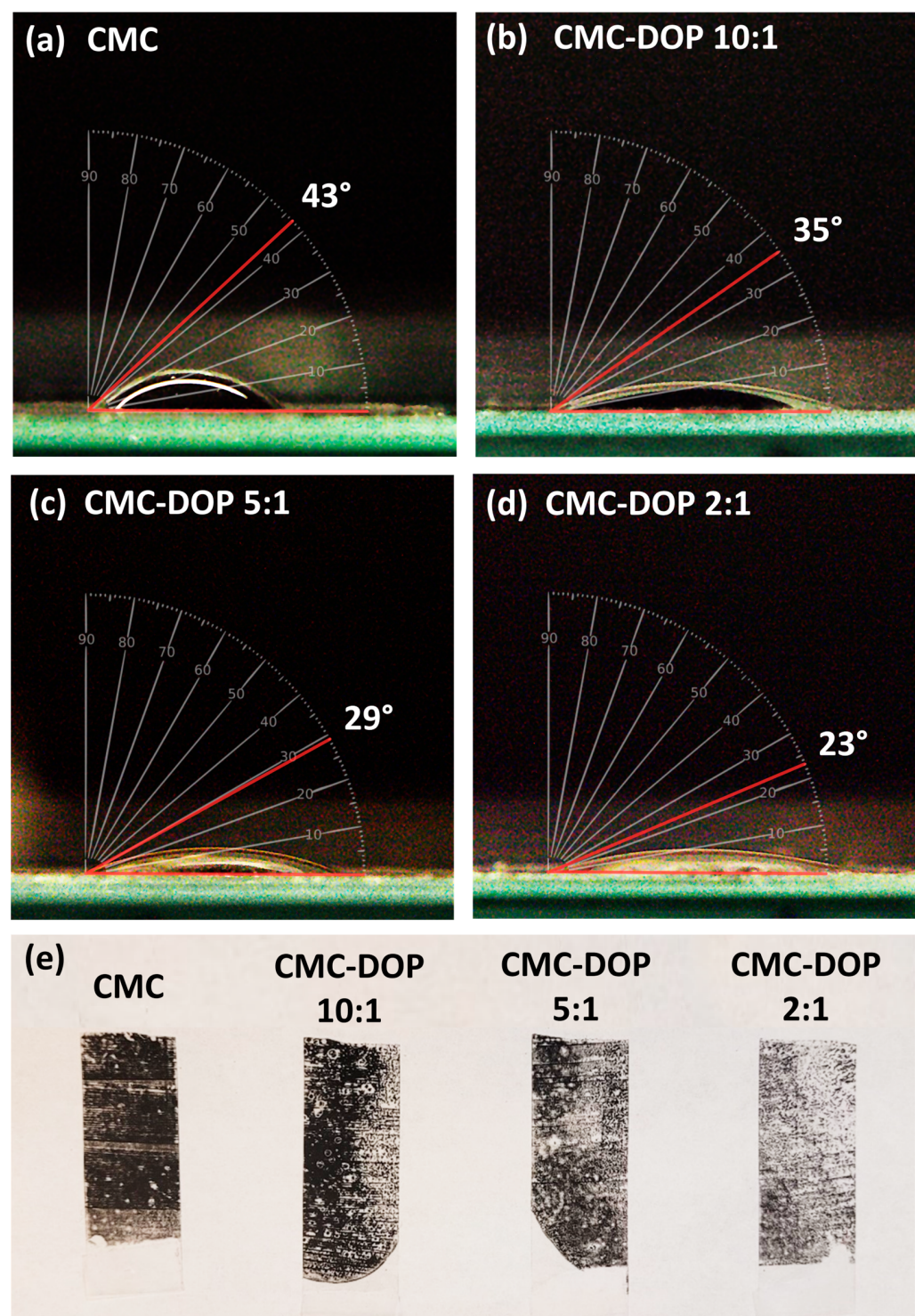


Figure 3. Contact-angle measurements for water dropped onto composite electrodes with (a) CMC, (b) CMC-DOP 10:1, (c) CMC-DOP 5:1, (d) and CMC-DOP 2:1 binders, respectively. (e) Tape peel measurements performed on prepared composite electrodes.

2.3. Electrochemistry

Coin-cell LSBs are cycled 500 times at C/5 rate with composite S/C cathode (Figure 4a) in Li metal anode. Specific capacity is reported with respect to the mass of active S material. Although the cell with the CMC-DOP 5:1 binder retains the highest specific capacity after 500 cycles, it is not highest initially, with cycle 1 showing capacities of 1058, 1083, 1045, and 870 mAh g⁻¹ for CMC and CMC-DOP 10:1, 5:1, and 2:1, respectively. A low capacity is

particularly observed for CMC-DOP 2:1. It is likely that the ether-insoluble NaCl coating of the electrode observed in Figure 2d hinders active material contact with the electrolyte and lowers the effective S utilization, despite its enhanced wettability. Between cycles 10 and 100, CMC-DOP 5:1 shows superior capacity retention. For CMC and CMC-DOP 10:1, 5:1, and 2:1, capacity retention between cycles 10 and 100 are 61.5, 63.9, 85.9, and 59.2%, respectively. CMC-DOP 10:1 performs similarly to the control CMC, suggesting low amounts of dopamine may be insufficient in markedly improving capacity. Conversely, CMC-DOP 2:1 shows exacerbated capacity fading, which is likely a symptom of corrosion and excess contamination with synthesis byproducts. Clearly a balance in these factors is required without additional purification.

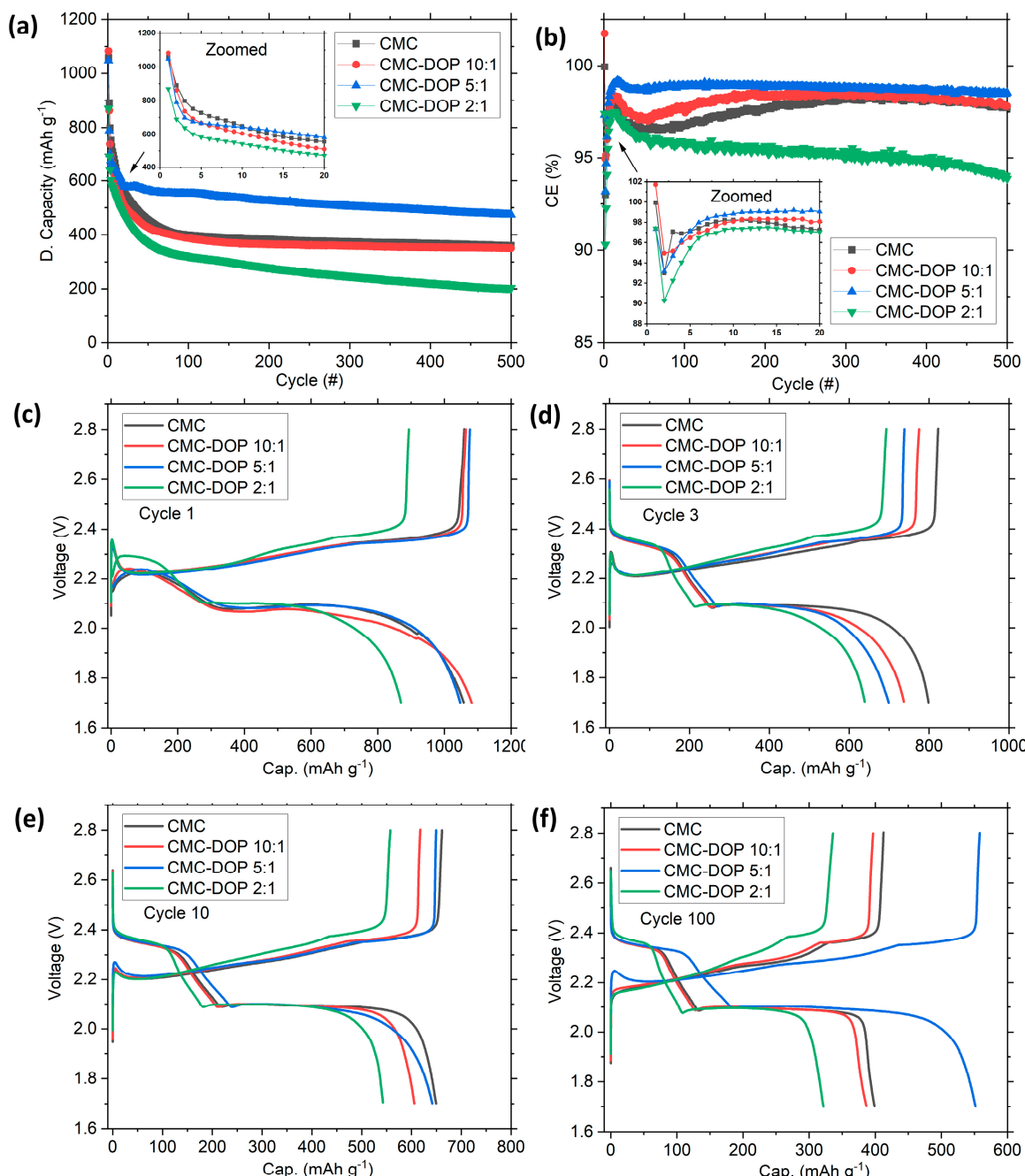


Figure 4. Constant current C/5 cycling of prepared LSBs with various binder compositions plotted as (a) discharge capacity and (b) CE versus cycle number. Select voltage profiles are represented from cycles (c) 1, (d) 3, (e) 10, and (f) 100.

CEs are also represented in Figure 4b for the cycling study, where $CE = \text{Discharge Capacity}/\text{Charge Capacity}$. Large changes in the CE and capacity are observed in the first 10 cycles as LiPSs initially dissolve into the electrolyte and S redistributes in the cathode or is lost to SEI formation [44]. After this period, the performance stabilizes. Over the initial 100 cycles, average CEs for CMC and CMC-DOP 10:1, 5:1, and 2:1 are 96.9, 97.5, 98.7, and 96.1%, respectively. The high CE for CMC-DOP 5:1 indicates that dopamine modification is successful in mitigating overcharging due to LiPS shuttling.

Select voltage profiles are also represented in Figure 4c. At the start of the initial discharge, there is dip due the activation barrier towards solubilizing S via electrochemical reactions [9,45]. For CMC and CMC-DOP 10:1, 5:1, and 2:1, this dip reaches 2.15, 2.17, 2.17, and 2.21 V, respectively. High wettability and enhanced electron transfer, which have been reported in PD/C composites for electronics, may lower this activation barrier [46]. The barrier is noticeably lower for CMC-DOP 2:1, suggesting that it initially enables lower impedance. This trend is mirrored in the first voltage plateau corresponding to the solid-to-liquid reaction of cyclic S_8 to form Li_2S_8 . At 50 mAh g^{-1} , the plateaus for CMC and CMC-DOP 10:1, 5:1, and 2:1 occur at 2.22, 2.24, 2.23, and 2.29 V.

In cycle 3 (Figure 4d), CMC provides the highest capacity, although this is not indefinitely maintained. By cycle 10 (Figure 4e), all cells give a similar capacity of $\sim 650 \text{ mAh g}^{-1}$ despite minor differences in the profiles. As in cycle 3, CMC-DOP 5:1 again shows greater capacity from the solid-to-liquid plateau between 2.4 and 2.1 V and the liquid-to-solid voltage drop-off of for Li_2S_2 precipitating into resistive Li_2S below 2.1 V. The sloping profile below 2.1 V for CMC-DOP 5:1 cycle 10 discharge also indicates more complete conversion of Li_2S_2 into Li_2S , demonstrating effective retention of the soluble species. Meanwhile, CMC derives a proportionately greater amount of capacity from the long, flat plateau at 2.1 V corresponding to the liquid-to-liquid reactions of Li_2S_8 reduction into Li_2S_4 and Li_2S_2 , suggesting excess LiPS generation. During charging there is an activation barrier to resolubilize insulating Li_2S . A large activation barrier additionally indicates a more complete reduction of soluble LiPSs into insoluble Li_2S . As such, during activation in cycle 10, the voltage peaks at 2.24, 2.25, 2.27, and 2.23 V for CMC and CMC-DOP 10:1, 5:1, and 2:1, respectively. These factors indicate that the CMC-DOP 5:1 binder most effectively retains soluble LiPSs, hindering their diffusion out of the porous cathode and increasing active material utilization [9,45].

The effect of successfully mitigated LiPS migration can be seen in cycle 100 (Figure 4f). By hindering active material loss to LiPS shuttling, CMC-DOP 5:1 maintains a high capacity of 552 mAh g^{-1} . Additionally, the sloping profile for Li_2S formation and the activation peak during charging can still be observed. Active material lost to shuttling will result in unfavorable passivation of the anode, causing high impedances. The smaller voltage hysteresis between the charge and discharge for CMC-DOP 5:1 suggests lower impedance and a more favorable SEI.

To provide additional mechanistic insight into SEI formation and observed performance, LSBs were removed after 500 cycles for electrochemical impedance spectroscopy (EIS). The resulting Nyquist plots for EIS spectra before and after cycling are shown in Figure 5a,b. To extract relevant parameters, spectra are fit to the equivalent circuit in Figure 5c. A resistor (R) in the high frequency region corresponds to bulk electrolyte (e) resistance. The two semicircles are fit using two sets of a constant phase element (CPE) and resistor in parallel to account for pseudocapacitance and resistance for interphase (int) contact in the bulk electrode at a high frequency (left) as well as the charge-transfer process (ct) and electric double-layer (dl) at the middle frequency (right) [47]. Another CPE at a low frequency represents diffusion (dif) in the electrolyte, although this is neglected in the fitting in Figure 5a due to poor convergence. A summary of all Z-fit parameters can be found in Tables S3 and S4.

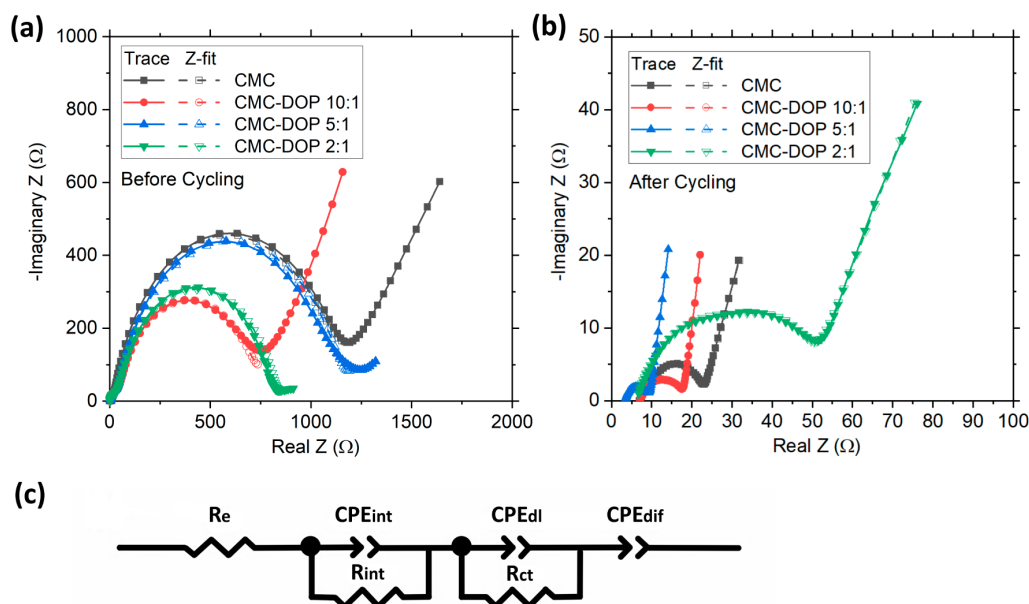


Figure 5. EIS spectra collected from LSBs (a) before and (b) after cycling study in Figure 4. Spectra are Z-fit using the equivalent circuit in (c).

Prior to cycling, low R_{ct} is observed for CMC-DOP 2:1 (Figure 5a). In excess, the dopamine precursor causes unfavorable physical properties and side reactions, leading to high R_{ct} by cycle 500. In Figure 5b, CMC-DOP 5:1 offers exceptionally low R_e and R_{ct} , showcasing the importance of electrode wettability at advanced cycle numbers. The lower R_e for CMC-DOP 5:1 may additionally indicate a lower polysulfide concentration in the electrolyte, which negatively impacts ionic conductivity [48]. Further, both CMC-DOP 10:1 and 5:1 facilitate lower R_{int} than the LSB with the CMC binder, further providing evidence of effective protection of the Li anode from LiPSs (Table 1). Overall, results correlate well with observed cycling performance and the proposed mechanism.

Table 1. Important Z-fit parameters from EIS spectra in Figure 5.

	Before			After		
	R_e (Ω)	R_{int} (Ω)	R_{ct} (Ω)	R_e (Ω)	R_{int} (Ω)	R_{ct} (Ω)
CMC	3.00	14.37	1104	7.05	2.49	14.12
CMC-DOP 10:1	2.98	34.91	693	7.01	1.30	9.56
CMC-DOP 5:1	3.94	27.99	1116	3.45	0.86	4.83
CMC-DOP 2:1	2.06	28.10	800	6.15	10.41	33.83

2.4. Post-Mortem Analysis

In LSBs, LiNO_3 additive alone is inadequate to protect the Li anode and maintain an effective SEI. LiPSs can be irreversibly reduced to Li_2S on the anode surface, forming a thick, resistive SEI which is more prone to fracturing and nucleation of dendrites [49]. In comparison to a dense, dendrite-free Li anode, this will further increase the anode surface area and exacerbate issues with SEI formation, electrolyte consumption, active material loss, and high impedance [50]. We therefore employed SEM/EDS imaging on the cycled LSB anodes and cathodes to investigate the impact of LiPS shuttling on the electrode morphology (Figure 6). A summary of quantitative EDS results can be found in Tables S5 and S6. The Li anode from LSB with the CMC binder shows an irregular morphology (Figure 6a). Some regions show dense Li, but in other areas, glob-like Li dendrites have formed, likely due to irregular Li deposition through the resistive SEI. White areas indicate charging effects from either electrically insulated dead Li or resistive Li_2S deposits. The cathode for the CMC binder cathode appears comparatively absent of

smoother S and instead reveals the barren C scaffold (Figure 6b). This is supported by quantitative EDS results showing a higher intensity for C (Table S5). CMC-DOP 10:1 anode shows a comparatively dense morphology with smaller Li globules and a cathode with smooth S on the surface (Figure 6c,d). The optimal morphology is observed for CMC-DOP 5:1, with Li densely packed into a regular morphology, indicating favorable SEI formation and even Li deposition (Figure 6e). The cathode similarly shows signs of excellent S retention (Figure 6f). Poorest Li morphology is observed for CMC-DOP 2:1, which shows large, irregular dendrites (Figure 6g). The cathode also reveals signs of degradation and large cracks due to corrosion of the foil (Figure 6h).

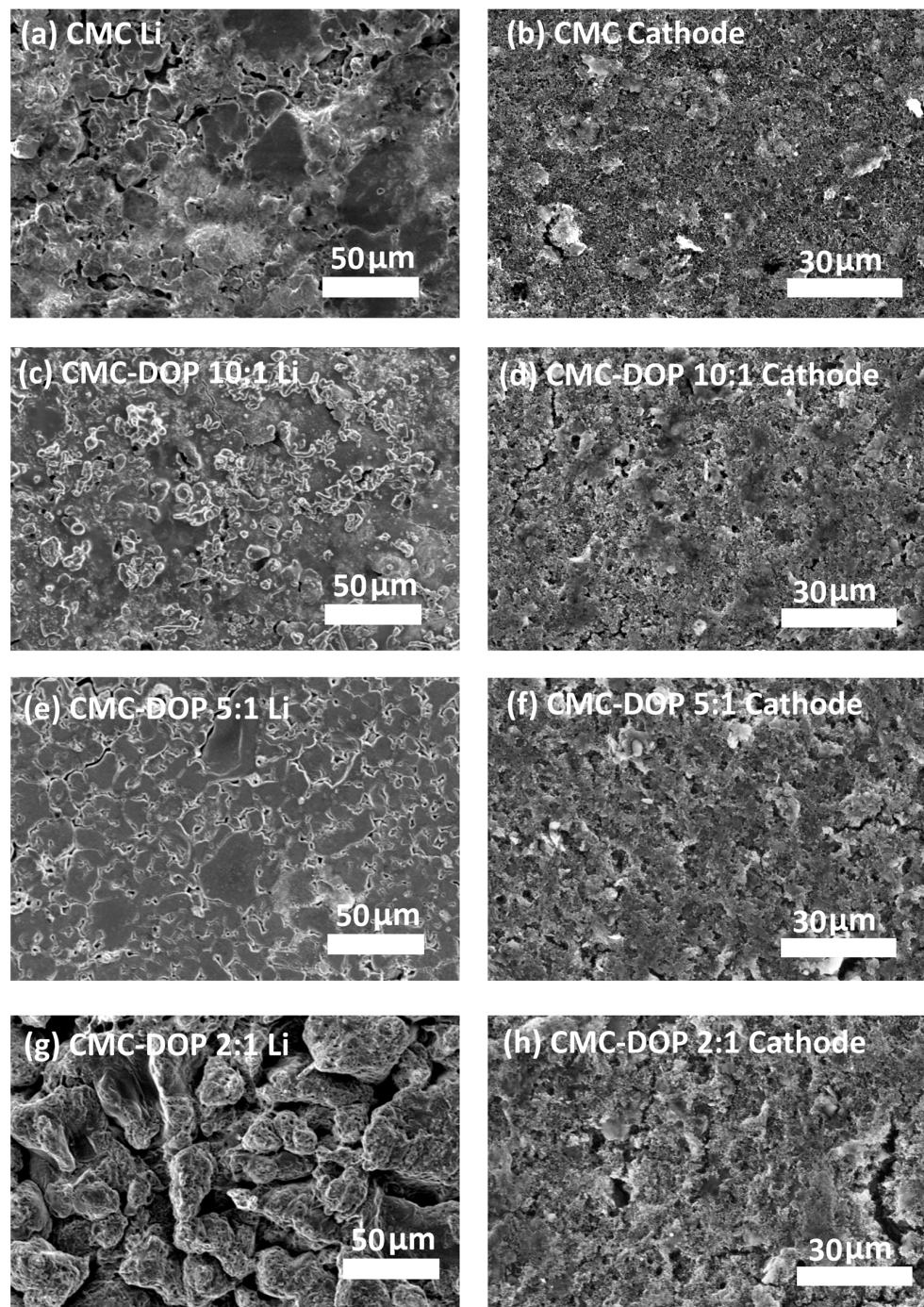


Figure 6. Post-cycled SEM images of (a,c,e,g) Li anode and (b,d,f,h) S cathodes of post mortem LSBs with (a,b) CMC, (c,d) CMC-DOP 10:1, (e,f) CMC-DOP 5:1, and (g,h) CMC-DOP 2:1 binders.

EDS quantitative S analyses in Figure 7 provide robust mechanistic support of conclusions from SEM and electrochemical tests. High CE, good capacity retention, low impedance, and dense Li morphology are correlated with low S wt.% at the anode and high S wt.% in the cathode. As such, CMC-DOP 5:1 shows the lowest S intensity at the anode and highest at the cathode. Quantitative S analysis for CMC and CMC-DOP 10:1, 5:1, and 2:1 cathodes show 5.85, 8.90, 12.15, and 3.25 wt.%, respectively (Table S5). Anode quantitative S analysis conversely reveals 19.09, 15.77, 13.82, and 30.18 wt.%, respectively (Table S6). Results for CMC-DOP 10:1 suggest effective LiPS retention despite comparable cycling performance to CMC. The mechanism for the lower-than-expected capacity may warrant further investigation. Analytical results overall, however, provide conclusive physical evidence of effective LiPS trapping via dopamine modification of CMC.

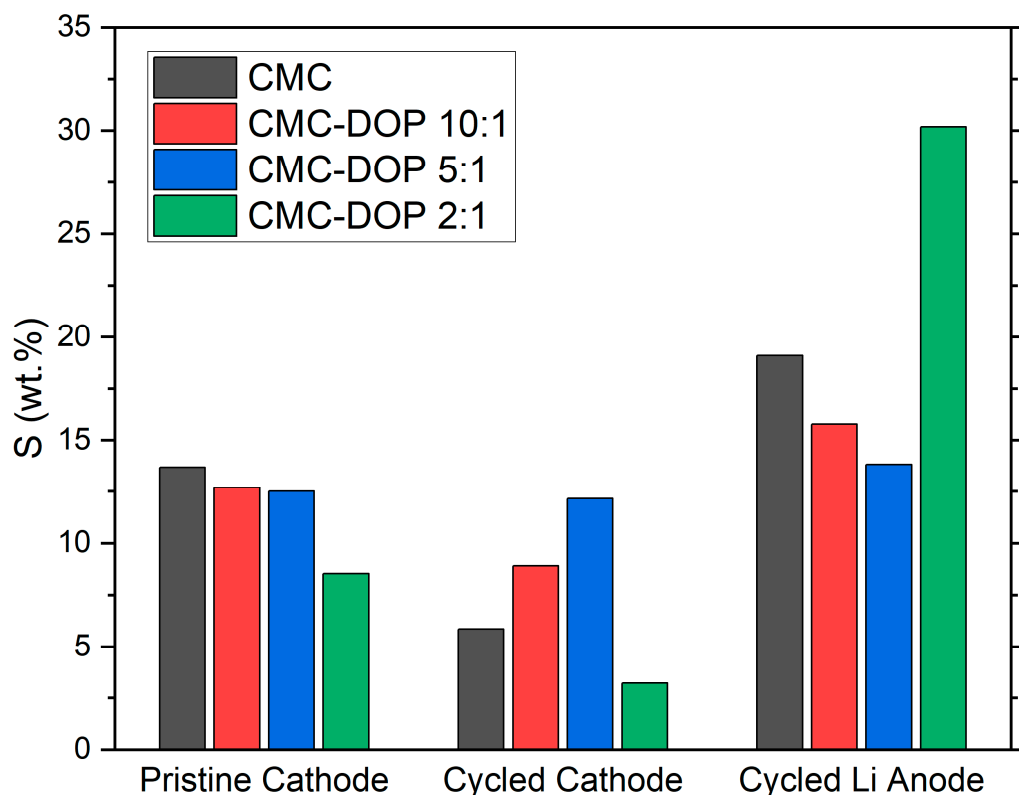


Figure 7. Quantitative S EDS results for LSB electrodes.

3. Conclusions

The dopamine-modified CMC-DOP binder exhibits exceptional electrochemical performance, providing a promising solution to the LiPS shuttling problem that hinders the commercialization of LSBs. This binder system is eco-friendly, inspired by nature, and easy to synthesize in a one-step amidation reaction. The results demonstrate the effectiveness of dopamine catechol functional groups in mitigating the LiPS shuttling effect. A ratio of 5:1 CMC to a dopamine precursor provides optimal performance, balancing the benefits of improved wettability, enhanced adhesion, and superior LiPS retention with the drawbacks of excess NaCl byproduct and current collector corrosion. The optimized CMC-DOP 5:1 binder outperforms the unmodified CMC, with a 38% improvement in capacity at cycle 100 to 552 mAh g⁻¹ and increased average CE from 96.9% to 98.7% over the same period. The prepared LSBs even retain a high efficiency after 500 cycles. Further optimization of the synthesis method has the potential to address the highlighted issues and could lead to LSBs becoming the next-generation battery technology, surpassing the limitations of LIBs. This binder may also be investigated in more sustainable and cost-effective sodium or potassium sulfur batteries, which similarly suffer from capacity loss due to polysulfide shuttling.

4. Materials and Methods

4.1. Synthesis

Na carboxymethyl cellulose modified with dopamine (CMC-DOP) is synthesized in a simple on-pot reaction. In a slurry cup, CMC (Aldrich, MW 700,000) and dopamine HCl (Fisher, 99%) precursor are combined and dissolved with 1000 mg of water in a planetary mixer (Thinky). For CMC-DOP 10:1, 5:1, and 2:1, the numbers represent weight ratios of CMC to the dopamine HCl precursor. The clear aqueous solution is then transferred to a sealed Teflon autoclave reactor and heated to 100 °C for 24 h. After this time, the solution turns a dark brown, indicating successful amidation. The CMC binder is prepared similarly, but without the addition of dopamine HCl or the heating step.

4.2. Electrode and Cell Preparation

S/C was composited by ball-milling 2 g of nanosulfur (SkySpring Nanomaterials, 99.99%, <55 nm) with 1 g of graphene nanopowder multilayer flakes (Graphene Supermarket, AO-4) for 30 min at 20 Hz, followed by sifting to 75 µm. The S/C composite was combined with carbon black (Timcal Super P) and the binder solution/dispersion at dry material weight ratios of 60:25:15, respectively. The mixture was homogenized in a planetary mixer for 30 min, blade-coated onto C-coated Al foil, and vacuum dried for 12 h at 45 °C. A 12 mm punch was used to make cathodes for coin cells. In an Ar glovebox (VAC) with H₂O and O₂ kept below 0.1 and 0.5 ppm, Li anodes were prepared by rolling Li rods (Aldrich, 99.9%) into a foil inside a polyethylene bag and hand punched into 14 mm disks. The electrolyte used for all cells was 1:1 by volume 1,3 dioxolane (DOL, Aldrich, anhydrous 99.8%) with cosolvent 1,2-dimethoxyethane (DME, Aldrich, anhydrous 99.5%) and salts 1 M bis(trifluoromethane)sulfonimide lithium (LiTFSI, Aldrich, anhydrous 99.99%) as well as 0.3 M LiNO₃ additive (Alfa Aesar, anhydrous 99%). Cells were assembled by layering electrodes in CR2032 coin casings (MTI) with Celgard 2500 separator and 25 µL of electrolyte inside an Ar glovebox.

4.3. Electrochemical Characterizations

The prepared LSB coin cells were cycled on an MTI BST8-3 Battery Analyzer. EIS was performed with a Gamry Reference 600 potentiostat. EIS was taken between 1 MHz and 1 Hz with a 10 mV amplitude.

4.4. Materials Characterizations

Scanning electron microscopy (SEM) images as well as energy dispersive spectroscopy (EDS) mapping and quantitative analysis of electrodes were provided by JEOL 600+ benchtop SEM. Cycled cathodes were soaked in 3 mL of DOL for 30 min and dried to remove residual salt prior to imaging and analysis. Fourier-transform infrared (FTIR) spectra were obtained using an Agilent Cary 630 spectrometer with diamond ATR. Nova Nano SEM 200 collected high-resolution SEM (HR-SEM) images of the prepared binders. Prior to imaging, the samples were cast onto Cu foil and Pt coated.

For tape-peel testing, cellulose tape (Scotch) was placed on top of the S/C composite electrode and adhered by rolling a 1 kg cylindrical weight over the surface. The tape was then peeled off, removing some of the composite electrode in the process.

Optical images for contact angle measurements were taken using a Nikon D3200 camera with a 55 mm lens and macro attachment.

Supplementary Materials: The following supporting information can be downloaded at: <https://www.mdpi.com/article/10.3390/batteries9110525/s1>.

Author Contributions: Conceptualization: D.A.G.; Methodology: D.A.G.; Drafting: D.A.G.; Funding: V.G.P.; Investigation: V.G.P.; Review: V.G.P. All authors have read and agreed to the published version of the manuscript.

Funding: V.G.P. and D.A.G. thank the National Science Foundation for supporting lithium sulfur battery research activities at Purdue University, IN under NSF-STTR-Phase II-20-546 grant.

Data Availability Statement: Data is available from the authors upon request.

Conflicts of Interest: The authors declare no conflict of interest.

References

- Rana, M.; Ahad, S.A.; Li, M.; Luo, B.; Wang, L.; Gentle, I.; Knibbe, R. Review on Areal Capacities and Long-Term Cycling Performances of Lithium Sulfur Battery at High Sulfur Loading. *Energy Storage Mater.* **2019**, *18*, 289–310. [[CrossRef](#)]
- Singh, A.N.; Kim, M.; Meena, A.; Wi, T.; Lee, H.; Kim, K.S. Na/Al Codoped Layered Cathode with Defects as Bifunctional Electrocatalyst for High-Performance Li-Ion Battery and Oxygen Evolution Reaction. *Small* **2021**, *17*, 2005605. [[CrossRef](#)]
- Liu, Y.-T.; Liu, S.; Li, G.-R.; Gao, X.-P. Strategy of Enhancing the Volumetric Energy Density for Lithium–Sulfur Batteries. *Adv. Mater.* **2021**, *33*, 2003955. [[CrossRef](#)] [[PubMed](#)]
- Etacheri, V.; Marom, R.; Elazari, R.; Salitra, G.; Aurbach, D. Challenges in the Development of Advanced Li-Ion Batteries: A Review. *Energy Environ. Sci.* **2011**, *4*, 3243–3262. [[CrossRef](#)]
- Cabana, J.; Monconduit, L.; Larcher, D.; Palacín, M.R. Beyond Intercalation-Based Li-Ion Batteries: The State of the Art and Challenges of Electrode Materials Reacting through Conversion Reactions. *Adv. Mater.* **2010**, *22*, 170–192. [[CrossRef](#)] [[PubMed](#)]
- Yang, L.; Li, Q.; Wang, Y.; Chen, Y.; Guo, X.; Wu, Z.; Chen, G.; Zhong, B.; Xiang, W.; Zhong, Y. A Review of Cathode Materials in Lithium-Sulfur Batteries. *Ionics* **2020**, *26*, 5299–5318. [[CrossRef](#)]
- Huang, Y.; Duan, J.; Zheng, X.; Wen, J.; Dai, Y.; Wang, Z.; Luo, W.; Huang, Y. Lithium Metal-Based Composite: An Emerging Material for Next-Generation Batteries. *Mater.* **2020**, *3*, 1009–1030. [[CrossRef](#)]
- Pan, H.; Cheng, Z.; He, P.; Zhou, H. A Review of Solid-State Lithium-Sulfur Battery: Ion Transport and Polysulfide Chemistry. *Energy Fuels* **2020**, *34*, 11942–11961. [[CrossRef](#)]
- Wild, M.; O'Neill, L.; Zhang, T.; Purkayastha, R.; Minton, G.; Marinescu, M.; Offer, G.J. Lithium Sulfur Batteries, a Mechanistic Review. *Energy Environ. Sci.* **2015**, *8*, 3477–3494. [[CrossRef](#)]
- Hu, Y.; Chen, W.; Lei, T.; Jiao, Y.; Huang, J.; Hu, A.; Gong, C.; Yan, C.; Wang, X.; Xiong, J. Strategies toward High-Loading Lithium–Sulfur Battery. *Adv. Energy Mater.* **2020**, *10*, 2000082. [[CrossRef](#)]
- Dysart, A.D.; Cardoza, N.A.; Mitchell, G.; Ortalan, V.; Pol, V.G. Effect of Synthesis Method Using Varying Types of Micropore Level Sulfur Infiltration on Electrochemical Performance in Lithium–Sulfur Batteries. *Energy Technol.* **2019**, *7*, 1900194. [[CrossRef](#)]
- Kim, P.J.; Fontecha, H.D.; Kim, K.; Pol, V.G. Toward High-Performance Lithium-Sulfur Batteries: Upcycling of LDPE Plastic into Sulfonated Carbon Scaffold via Microwave-Promoted Sulfonation. *ACS Appl. Mater. Interfaces* **2018**, *10*, 14827–14834. [[CrossRef](#)] [[PubMed](#)]
- Hong, C.N.; Kye, D.K.; Mane, A.U.; Elam, J.W.; Etacheri, V.; Pol, V.G. Blocking Polysulfides in Graphene–Sulfur Cathodes of Lithium–Sulfur Batteries through Atomic Layer Deposition of Alumina. *Energy Technol.* **2019**, *7*, 1900621. [[CrossRef](#)]
- Lee, J.; Choi, W. Surface Modification of Sulfur Cathodes with PEDOT:PSS Conducting Polymer in Lithium-Sulfur Batteries. *J. Electrochem. Soc.* **2015**, *162*, A935–A939. [[CrossRef](#)]
- Parekh, M.H.; Rao, H.; Jokhakar, D.; Parikh, V.P.; Palanisamy, M.; Pol, V.G. Polysulfide Shuttle Mitigation through a Tailored Separator for Critical Temperature Energy-Dense Lithium-Sulfur Batteries. *Sustain. Energy Fuels* **2022**, *6*, 5591–5599. [[CrossRef](#)]
- Gribble, D.A.; Lin, Z.Y.; Ghosh, S.; Savoie, B.M.; Pol, V.G. Mitigating Polysulfide Shuttles with Upcycled Alkali Metal Terephthalate Decorated Separators. *Batteries* **2022**, *8*, 253. [[CrossRef](#)]
- Wei, Z.; Ren, Y.; Sokolowski, J.; Zhu, X.; Wu, G. Mechanistic Understanding of the Role Separators Playing in Advanced Lithium-sulfur Batteries. *InfoMat* **2020**, *2*, 483–508. [[CrossRef](#)]
- Gribble, D.A.; McCulfor, E.; Li, Z.; Parekh, M.; Pol, V.G. Enhanced Capacity and Thermal Safety of Lithium-Ion Battery Graphite Anodes with Conductive Binder. *J. Power Sources* **2023**, *553*, 232204. [[CrossRef](#)]
- Gribble, D.A.; Li, Z.; Ozdogru, B.; McCulfor, E.; Çapraz, Ö.; Pol, V.G. Mechanistic Elucidation of Electronically Conductive PEDOT:PSS Tailored Binder for a Potassium-Ion Battery Graphite Anode: Electrochemical, Mechanical, and Thermal Safety Aspects. *Adv. Energy Mater.* **2022**, *12*, 2103439. [[CrossRef](#)]
- Yuan, H.; Huang, J.Q.; Peng, H.J.; Titirici, M.M.; Xiang, R.; Chen, R.; Liu, Q.; Zhang, Q. A Review of Functional Binders in Lithium–Sulfur Batteries. *Adv. Energy Mater.* **2018**, *8*, 1802107. [[CrossRef](#)]
- Li, Y.; Zeng, Q.; Gentle, I.R.; Wang, D.W. Carboxymethyl Cellulose Binders Enable High-Rate Capability of Sulfurized Polyacrylonitrile Cathodes for Li-S Batteries. *J. Mater. Chem. A* **2017**, *5*, 5460–5465. [[CrossRef](#)]
- Zhang, Z.; Bao, W.; Lu, H.; Jia, M.; Xie, K.; Lai, Y.; Li, J. Water-Soluble Polyacrylic Acid as a Binder for Sulfur Cathode in Lithium-Sulfur Battery. *ECS Electrochem. Lett.* **2012**, *1*, A34. [[CrossRef](#)]
- Pan, J.; Xu, G.; Ding, B.; Chang, Z.; Wang, A.; Dou, H.; Zhang, X. PAA/PEDOT:PSS as a Multifunctional, Water-Soluble Binder to Improve the Capacity and Stability of Lithium-Sulfur Batteries. *RSC Adv.* **2016**, *6*, 40650–40655. [[CrossRef](#)]
- Pang, Z.; Zhang, H.; Ma, Y.; Song, D.; Shi, X.; Zhang, L.; Zhou, Y. Polyglutamic Acid Binder for High-Performance Lithium–Sulfur Batteries. *Coatings* **2022**, *12*, 1433. [[CrossRef](#)]
- Versaci, D.; Nasi, R.; Zubair, U.; Amici, J.; Sgroi, M.; Dumitrescu, M.A.; Francia, C.; Bodoardo, S.; Penazzi, N. New Eco-Friendly Low-Cost Binders for Li-Ion Anodes. *J. Solid State Electrochem.* **2017**, *21*, 3429–3435. [[CrossRef](#)]

26. Dong, Q.; Zhang, X.; Qian, J.; He, S.; Mao, Y.; Brozena, A.H.; Zhang, Y.; Pollard, T.P.; Borodin, O.A.; Wang, Y.; et al. A Cellulose-Derived Supramolecule for Fast Ion Transport. *Sci. Adv.* **2022**, *8*, eadd2031. [[CrossRef](#)]
27. Xu, L.; Meng, T.; Zheng, X.; Li, T.; Brozena, A.H.; Mao, Y.; Zhang, Q.; Clifford, B.C.; Rao, J.; Hu, L. Nanocellulose-Carboxymethylcellulose Electrolyte for Stable, High-Rate Zinc-Ion Batteries. *Adv. Funct. Mater.* **2023**, *33*, 2302098. [[CrossRef](#)]
28. Liu, W.; Lin, D.; Pei, A.; Cui, Y. Stabilizing Lithium Metal Anodes by Uniform Li-Ion Flux Distribution in Nanochannel Confinement. *J. Am. Chem. Soc.* **2016**, *138*, 15443–15450. [[CrossRef](#)]
29. Hollingshead, S.; Torres, J.E.; Wilker, J.J.; Liu, J.C. Effect of Cross-Linkers on Mussel- and Elastin-Inspired Adhesives on Physiological Substrates. *ACS Appl. Bio Mater.* **2022**, *5*, 630–641. [[CrossRef](#)]
30. Deng, Y.; Xu, H.; Bai, Z.; Huang, B.; Su, J.; Chen, G. Durable Polydopamine-Coated Porous Sulfur Core-Shell Cathode for High Performance Lithium-Sulfur Batteries. *J. Power Sources* **2015**, *300*, 386–394. [[CrossRef](#)]
31. Della Vecchia, N.F.; Luchini, A.; Napolitano, A.; Derrico, G.; Vitiello, G.; Szekely, N.; Dischia, M.; Paduano, L. Tris Buffer Modulates Polydopamine Growth, Aggregation, and Paramagnetic Properties. *Langmuir* **2014**, *30*, 9811–9818. [[CrossRef](#)] [[PubMed](#)]
32. Pettignano, A.; Charlot, A.; Fleury, E. Solvent-Free Synthesis of Amidated Carboxymethyl Cellulose Derivatives: Effect on the Thermal Properties. *Polymers* **2019**, *11*, 1227. [[CrossRef](#)] [[PubMed](#)]
33. Mansouri, L.; Elkolli, M.; Zohra, B. Effect of Acidification on Biological Proprieties of Sodium Carboxymethylcellulose HCl/EtOH. *Mater. Biomater. Sci.* **2020**, *3*, 65–70.
34. Wang, Z.; Huang, T.; Liu, Z.; Yu, A. Dopamine-Modified Carboxymethyl Cellulose as an Improved Aqueous Binder for Silicon Anodes in Lithium-Ion Batteries. *Electrochim. Acta* **2021**, *389*, 138806. [[CrossRef](#)]
35. Liebscher, J. Chemistry of Polydopamine—Scope, Variation, and Limitation. *Eur. J. Org. Chem.* **2019**, *2019*, 4976–4994. [[CrossRef](#)]
36. Chhatwal, A.R.; Lomax, H.V.; Blacker, A.J.; Williams, J.M.J.; Marcé, P. Direct Synthesis of Amides from Nonactivated Carboxylic Acids Using Urea as Nitrogen Source and Mg(NO₃)₂ or Imidazole as Catalysts. *Chem. Sci.* **2020**, *11*, 5808–5818. [[CrossRef](#)]
37. Thakur, A.; Ranote, S.; Kumar, D.; Bhardwaj, K.K.; Gupta, R.; Chauhan, G.S. Synthesis of a PEGylated Dopamine Ester with Enhanced Antibacterial and Antifungal Activity. *ACS Omega* **2018**, *3*, 7925–7933. [[CrossRef](#)] [[PubMed](#)]
38. Gagić, T.; Perva-Uzunalić, A.; Knez, Ž.; Škerget, M. Hydrothermal Degradation of Cellulose at Temperature from 200 to 300 °C. *Ind. Eng. Chem. Res.* **2018**, *57*, 6576–6584. [[CrossRef](#)]
39. Zheng, W.; Fan, H.; Wang, L.; Jin, Z. Oxidative Self-Polymerization of Dopamine in an Acidic Environment. *Langmuir* **2015**, *31*, 11671–11677. [[CrossRef](#)]
40. Egbuhuzor, O.M.; Madufor, I.C.; Nwanonenyi, S.C.; Bokolo, J.O. Adsorption Behavior and Corrosion Rate Model of Sodium Carboxymethyl Cellulose (Na-CMC) Polymer on Aluminium in HCl Solution. *Niger. J. Technol.* **2020**, *39*, 369–378. [[CrossRef](#)]
41. Sheng, Y.; Fell, C.R.; Son, Y.K.; Metz, B.M.; Jiang, J.; Church, B.C. Effect of Calendering on Electrode Wettability in Lithium-Ion Batteries. *Front. Energy Res.* **2014**, *2*, 56. [[CrossRef](#)]
42. Fu, L.J.; Endo, K.; Sekine, K.; Takamura, T.; Wu, Y.P.; Wu, H.Q. Studies on Capacity Fading Mechanism of Graphite Anode for Li-Ion Battery. *J. Power Sources* **2006**, *162*, 663–666. [[CrossRef](#)]
43. Choi, J.W.; Aurbach, D. Promise and Reality of Post-Lithium-Ion Batteries with High Energy Densities. *Nat. Rev. Mater.* **2016**, *1*, 16013. [[CrossRef](#)]
44. Liu, J.; Zheng, Y. Dissolution and Reprecipitation of Sulfur on Carbon Surface. *J. Electron. Mater.* **2022**, *51*, 2926–2932. [[CrossRef](#)]
45. Zhang, S.S. Liquid Electrolyte Lithium/Sulfur Battery: Fundamental Chemistry, Problems, and Solutions. *J. Power Sources* **2013**, *231*, 153–162. [[CrossRef](#)]
46. Jin, Z.; Yang, L.; Shi, S.; Wang, T.; Duan, G.; Liu, X.; Li, Y. Flexible Polydopamine Bioelectronics. *Adv. Funct. Mater.* **2021**, *31*, 2103391. [[CrossRef](#)]
47. Deng, Z.; Zhang, Z.; Lai, Y.; Liu, J.; Li, J.; Liu, Y. Electrochemical Impedance Spectroscopy Study of a Lithium/Sulfur Battery: Modeling and Analysis of Capacity Fading. *J. Electrochem. Soc.* **2013**, *160*, A553–A558. [[CrossRef](#)]
48. Fan, F.Y.; Pan, M.S.; Lau, K.C.; Assary, R.S.; Woodford, W.H.; Curtiss, L.A.; Carter, W.C.; Chiang, Y.-M. Solvent Effects on Polysulfide Redox Kinetics and Ionic Conductivity in Lithium-Sulfur Batteries. *J. Electrochem. Soc.* **2016**, *163*, A3111–A3116. [[CrossRef](#)]
49. Huang, L.; Li, J.; Liu, B.; Li, Y.; Shen, S.; Deng, S.; Lu, C.; Zhang, W.; Xia, Y.; Pan, G.; et al. Electrode Design for Lithium–Sulfur Batteries: Problems and Solutions. *Adv. Funct. Mater.* **2020**, *30*, 1910375. [[CrossRef](#)]
50. Bouchet, R.; Maria, S.; Meziane, R.; Aboulaich, A.; Lienafa, L.; Bonnet, J.; Phan, T.N.T.; Bertin, D.; Gigmes, D.; Devaux, D.; et al. Efficient Electrolytes for Lithium-Metal Batteries. *Nat. Mater.* **2013**, *12*, 452–457. [[CrossRef](#)]

Disclaimer/Publisher’s Note: The statements, opinions and data contained in all publications are solely those of the individual author(s) and contributor(s) and not of MDPI and/or the editor(s). MDPI and/or the editor(s) disclaim responsibility for any injury to people or property resulting from any ideas, methods, instructions or products referred to in the content.